Atmospheric
Chemistry
and Physics

Supplement of

Mass spectrometric analysis of unprecedented high levels of carbonaceous aerosol particles long-range transported from wildfires in the Siberian Arctic

Eric Schneider et al.

Correspondence to: Hendryk Czech (hendryk.czech@uni-rostock.de)

S1. Study area – Wildfires in Siberia

Siberia is a vast Russian province encompassing most of Northern Asia, (see map in Fig.1), with terrain spanning tundra and coniferous forest. The Siberian forest is divided into the "dark taiga" in the West and "light taiga" in the East, owing to the brightness of the dominating vegetation. While the light taiga is mainly comprised of larch species, the dark Taiga is home to species of spruce and fir. The genus of pine is present in the entire forest, whereas the abundance of deciduous tree like birch and poplar is restricted to the South (Kharuk et al., 2021). This composition determines the frequency and intensity of wildfires as different tree species have different strategies to deal with fires. Both pine and larch belong to the class of "resistors", surviving small and medium fires due to their thick bark, and tolerating frequent surface fires, which deploy fuels like duff, loose needles, herbaceous vegetation and growth-restricted plants. In contrast, many spruce and fir species dominating in the dark Taiga have dense canopies that protect the ground from drying and thus reduce ignition ability (Tautenhahn et al., 2016).

The ignition of a wildfire often starts with dead vegetation on the ground, such as litter or duff, and spread to the understory. Such surface fires may induce crown fires and set canopies in flames. Crown fires used to appear in parallel to surface fire, however, they may have the same or different fire fronts (Northwest Fire Science Consortium). In the opposite vertical direction of the fire spread to the canopy, ground fires consuming duff, decayed roots and peat as fuel, can persist over long times with a continuous moderate to low smoke release (Popovicheva et al., 2019).

Due to a large size and continuous production, gas flaring of oil industry is one of the highest BC emission sources with a strong environmental and climatic impact for the Arctic(Cho et al., 2019). North of Western Siberia is an industrially - developed region with a leading oil and gas production industry and the world's largest gas flaring region (Fig.1). The contribution of gas flaring from the YNAO, KMAO, and Komi Republic to the annual total Arctic surface BC composes 31% (Zhu et al., 2020). Observations of plumes from gas flaring regions over the Kara Sea proved an impact of BC long-range transport from Siberia (Popovicheva et al., 2017). Bely Island takes place in the Kara Sea, above Yamal Peninsula, north of the YNAO (Fig. 1). Here, at the air pathway of large-scale emission plumes from populated industrial regions of Eurasia and of wildfires to the Arctic, the polar research aerosol station "Island Bely" of MSU was installed and operated since 2019 (Popovicheva et al., 2022).

Particularly the fire season in 2021 in Yakutia was recognized to have a high severity and increased emissions of fine particulate matter (PM2.5) by 75% compared to the total federal

subjects (Romanov et al., 2022), caused by persistent anticyclones. The high barometric pressure promoted dry weather conditions in the region by blocking the transport of moist air masses from the western part of Russia. Additionally, low wind speed let emissions accumulate to extremely dense plumes (Tomshin and Solovyev, 2018).

According to the operational data of Avialesokhrana (https://aviales.ru/), 105 wildfires were active on an area of about 1.2 million hectares in Yakutia in August 2021. On 04 to 08 August 2021 smoke enveloped cites of the YNAO district. On 04 August 2021, strong smoke covered Nadym city, located around 100 km to the south the Polar Circle (Fig.1). On the 06 August 2021, residents of other cities and villages of YNAO suffered with the smell of burning. High smoke pollution was recorded by polar aerosol station "Island Bely" on Bely Island.

S2. Detailed Experimental Section

S2.1 Filter Extraction

One-half of each quartz fiber filter was placed in a cleaned extraction vial with 8 mL of a methanol and dichloromethane (1:1 v/v, LC-MS grade) mixture. After extraction for 20 min in an ice-chilled ultra-sonic bath, the extract was filtered through a PTFE membrane (0.2 μm, Sartorius) in a stainless-steel filter holder via a cleaned glass syringe. Filter and laboratory blanks were extracted in the same way. Filtered extracts were immediately stored at -25 °C until further analysis. Finally, extracts were diluted to a concentration of approx. 10 μg OC mL^{-1} by addition of a methanol and dichloromethane mixture (1:1 v/v) directly prior to analysis.

S2.2 Ion Source Settings: APPI/ESI

The following ionization parameter were selected for positive/negative ion mode (ESI+/-) respectively: Capillary voltage -3.4/3.5 kV, drying gas temperature 180 °C, drying gas flow rate 4.0 L min^{-1}, nebulizer gas flow rate 1.4 bar, and syringe flow rate 200 μL h^{-1}. For each measurement, 400 scans were collected in the range of 150–1,000 Da in magnitude mode, with a 1.96 s (4M) transient, a resulting resolving power of >310,000 at m/z 400 and mass accuracy below 1 ppm. For APPI the source parameters were set to: drying gas temperature 220 °C, drying gas flow rate 4.0 L min^{-1}, nebulizer gas flow rate 2.5 bar vaporizer temperature 370°C, and a syringe flow rate of 500 μL h^{-1}.

S2.3 Resonance-Enhanced Multi photon Ionization

The fourth harmonic generation of the fundamental radiation of a Nd:YAG laser (Big Sky Ultra; Quantel, France) was used for REMPI at 266 nm with subsequent ion detection by a TOFMS (compact mass spectrometer II; Firma Stefan Kaesdorf, Germany) (Miersch et al., 2019a). As REMPI is conducted under vacuum conditions, the intensity of an analyte is linearly proportional to its concentration in contrast to direct injection of samples and ionization under atmospheric pressure conditions, such as ESI or APPI. At 266 nm and moderate laser fluence, REMPI is particularly sensitive for PAHs, however, photoionization cross sections may differ between individual PAH isomers. An overview on REMPI photoionization cross sections is given by Gehm et al., Haeflinger et al. and Streibel et al. (Gehm et al., 2018; Haefliger and Zenobi, 1998; Streibel et al., 2006).

S2.4 Molecular Properties Calculation

Formulae applied for the calculation of double bond equivalents (DBE), aromaticity index (AI, modified for high oxygen content) (Koch and Dittmar, 2006), average carbon oxidation state (OS_C) (Kroll et al., 2011), saturation vapour pressure (C^*, Table S2)(Li et al., 2016b) and maximum carbonyl ratio (MCR) (Zhang et al., 2021). Calculations are based on the assigned neutral sum formulae $C_cH_hN_nO_oS_s$.

$$DBE = c - \frac{h}{2} + \frac{n}{2} + 1 \tag{1}$$

$$AI = \frac{1 + c - 0.5\,o - s - 0.5\,h}{c - 0.5\,o - s - n} \tag{2}$$

$$\overline{OS_C} = 2\frac{o}{c} - \frac{h}{c} \tag{3}$$

$$\log_{10} C^* = (n_c^0 - c)b_c - ob_o - 2\frac{c\,o}{c+o}b_{co} - nb_n - sb_s \tag{4}$$

$$MCR = \frac{DBE}{o}\ (o \geq DBE)\ else\ MCR = 1 \tag{5}$$

Organic aerosol compounds can be classified into five groups, based on their saturation vapor pressure (C^*): volatile organic compounds (VOC; $C^* > 3 \times 10^6$ µg m^{-3}), intermediate volatility OC (IVOC; $300 < C^* < 3 \times 10^6$ µg m^{-3}), semi volatile OC (SVOC; $0.3 < C^* < 300$ µg m^{-3}), low-volatile OC (LVOC; $3 \times 10^{-4} < C^* < 0.3$ µg m^{-3}), and extremely low-volatile OC (ELVOC; $C^* < 3 \times 10^{-4}$ µg m^{-3}) (Li et al., 2016a; Donahue et al., 2011).

S3 Selectivity of APPI and ESI

Although there is a significant overlap of identified sum formulae (Fig. S3), each ionization technique covers its specific chemical space. While APPI shows higher sensitivity for the ionization of low polarity compounds (analyte ionization energy lower than photon energy of 10.6 eV), ESI is more sensitive for the detection of high polarity compounds. With ESI+ basic polar functional groups (strong ability to form hydrogen/sodium-adducts) are selectively ionized, while ESI- is focused on acidic polar functional groups (deprotonation). Based on the selectivity, differences between the spectra of ESI+ and ESI- can be used to gain insights of the molecular structure of detected sum formulae. For example, carbonyl, nitro or nitrooxy groups are easily ionized by ESI+, while in ESI- carboxyl, hydroxyl or sulfate moieties are preferred.

S4 Ratio of Primary Retene to Total Retene

In order to test the validity of the RET_{prim}/RET_{pyr} approach, TOCA-REMPI-TOFMS measurements from spruce logwood combustion in two modern wood stoves were reinvestigated (Czech et al., 2018; Miersch et al., 2019b). As expected, ratios of RET_{prim} to RET_{tot} were larger than for the Yakutian wildfire plume sampled in Nadym city. However, during long-range transport, the wildfire plume has undergone atmospheric ageing, which likely affect the ratio of RET_{prim} to RET_{pyr}, but to an unknown extent. Additionally, wood combustion samples were collected in a previous study at a dilution of 30, which is distinct different from the dilution wildfire aerosol receives in ambient air and shifts the partitioning of semi-volatile species like retene to the particle phase. In one experiment with spruce logwood, the first batch did not ignite properly (Czech et al., 2016) and caused significantly higher emissions of primary resin constituents or earlier thermal alteration products identified by *in situ* derivatization thermal desorption gas chromatography mass spectrometry (Czech et al., 2018). While all eight normal combustion experiments led to RET_{prim}/RET_{tot} of 0.67±0.13, this single experiment yield in a distinct lower RET_{prim}/RET_{tot} of 0.26 under the same dilution conditions (Table S8).

Furthermore, retene refers to a semi-volatile PAH and may be processed by both gas phase and particle phase reactions with atmospheric oxidants, other particle constituents or by photolysis. For the latter atmospheric fate, the composition of the particles plays a crucial role for degradation kinetics (Douben, 2003). It has been found that dehydroabietic acid, a thermal alteration product from abietic acid, partitions more in the particle phase than retene and its atmospheric lifetime due to OH radicals was estimated between 2.3 and 4.5 days depending on

temperature, humidity and particle composition (Lai et al., 2015). However, first oxidation products of diterpenoids may similarly degraded as diterpenoids released from BB, hence still contributing to RET_{pyr} despite oxidation. Although rate constants toward OH in the same order of magnitude for PAH of similar vapor pressure like retene, the dataset of this study cannot confirm the validity of the RET_{prim}/RET_{pyr} approach for longer residence times in the atmosphere. Nevertheless, a conserved ratio of RET_{prim} and RET_{pyr} in dense BB plumes with high OH reactivity is plausible because of an OH deficit (Decker et al., 2021), high optical thickness and organic coating possibly protecting polyaromatic compounds from photolysis.

Table S1: Filter sampling parameters for samples collected in Nadym city and on Bely Island in August 2021 including date, duration, volume, EC and OC fractions according to Improve_A protocol. Samples combined for FT-ICR MS data discussion highlighted in green and sample from Bely Island collected during the same period highlighted in blue.

sample Nadym	date	start time (UTC+3)	end time (UTC+3)	volume [m³]	OC1	OC2	OC3	OC4	OC pyro	EC1	EC2	EC3	OC total	EC total
					[µg m⁻³]									
N01	21-08-05	13:34	17:52	19.21	2.2	5.7	11.4	4.4	9.5	10.9	0.3	0.0	33.2	11.2
N02	21-08-06	06:03	15:06	38.47	2.6	7.7	8.9	1.3	11.8	13.0	0.3	0.0	32.4	13.3
N03	21-08-07	09:20	12:22	12.96	8.5	20.0	27.7	7.8	34.8	39.1	0.6	0.0	98.7	39.8
N04	21-08-07	13:39	16:24	11.69	8.5	19.1	26.3	6.5	38.5	50.7	0.5	0.0	98.9	51.2
N05	21-08-07	17:34	23:49	25.73	4.1	10.0	14.3	4.2	16.3	19.6	0.2	0.0	49.0	19.8
N07	21-08-08	08:39	15:35	29.4	0.9	3.4	6.3	3.1	6.8	10.6	0.1	0.0	20.5	10.7
N08	21-08-08	16:39	21:39	21.54	0.1	0.7	2.1	1.0	1.5	1.7	0.0	0.0	5.4	1.7
N09	21-08-09	12:19	23:59	51.61	0.0	0.2	0.2	0.1	0.1	0.1	0.0	0.0	0.7	0.1
N10	21-08-12	06:57	17:26	44.52	0.2	0.8	1.5	0.7	0.5	1.0	0.2	0.0	3.7	1.2

sample Bely	start time (UTC+3)	end time (UTC+3)	volume [m³]	OC1	OC2	OC3	OC4	OC pyro	EC1	EC2	EC3	OC total	EC total
				[µg m⁻³]									
B01	21-07-31 10:44	21-08-07 08:12	357.1	1.5	1.6	2.4	0.4	3.0	0.2	0.1	0.0	8.9	0.3
B02	21-08-07 08:25	21-08-14 09:18	361.3	0.5	1.1	1.2	0.3	0.9	0.3	0.0	0.0	3.9	0.3
B03	21-08-14 09:23	21-08-21 09:35	358.6	0.0	0.1	0.2	0.1	0.1	0.0	0.0	0.0	0.5	0.0

Table S2: Compound classes and their respective n^0_C and b values from Li et al. (Li et al., 2016b) obtained by least-squares optimization using compounds from the NCI database.

Compound class	n^0_C	b_c	b_o	b_{co}	b_n	b_s
CH	23.8	0.4861				
CHO	22.66	0.4481	1.656	−0.7790		
CHN	24.59	0.4066			0.9619	
CHNO	24.13	0.3667	0.7732	−0.07790	1.114	
CHOS	24.06	0.3637	1.327	−0.3988		0.7579
CHNOS	28.5	0.3848	1.011	0.2921	1.053	1.316

Table S3: Intensity weighted average sum parameter of main wildfire impacted samples (N01-N05) at Nadym and exemplary ambient aerosol sample from Nadym (N09).

Sum parameter	N01-N05 (averaged) intensity weighted average			N09 intensity weighted average		
	APPI	ESI-	ESI+	APPI	ESI-	ESI+
sum formula number	5522	4180	6436	301	2560	2635
OSc	-0.81	-0.49	-1.09	-1.19	-0.78	-1.24
DBE	7.78	7.42	4.99	4.80	5.66	3.54
AI	0.24	0.17	0.10	0.17	0.15	0.07
log(C*)	-4.70	-7.03	-4.94	-2.37	-4.32	-3.93
OM/OC	2.76	2.96	3.03	2.87	3.01	3.13
H/C	1.42	1.44	1.69	1.63	1.57	1.82
O/C	0.31	0.48	0.31	0.23	0.40	0.29
N/C	0.07	0.08	0.06	0.12	0.07	0.07
S/C	0.04	0.05	0.04	0.05	0.06	0.04
O/N	5.91	7.18	4.78	3.12	6.11	4.35
O/S	11.22	9.46	6.14	10.69	7.24	3.38
C	23.70	22.02	24.22	22.32	20.48	22.97
H	34.47	31.95	41.14	37.39	32.27	41.35
N	0.63	0.75	0.68	0.33	0.62	0.48
O	6.45	9.57	6.45	4.04	7.18	6.04
S	0.01	0.13	0.03	0.05	0.13	0.14
m/z	432.60	463.30	462.34	377.45	408.06	444.80

Table S4: Relative Intensity of sum formula of average main wildfire impacted samples and ambient from Nadym, separated into Maximum Carbonyl ratio (MCR) areas.

MCR area	class limits		N01-N05 relative Intensity [%]			N08-N10 relative Intensity [%]		
	MCR	AI	APPI	ESI-	ESI+	APPI	ESI-	ESI+
very highly oxidized	0-0.2	-	0.2	0.2	10.4	2.79	7.19	41.29
highly oxidized	0.2-0.5	-	9.4	18.9	35.8	10.93	27.71	34.15
intermediately oxidized	0.5-0.9	-	21.2	47.0	28.6	23.93	44.06	15.22
oxidized unsaturated	0.9-1	< 0.5	63.3	31.4	25.1	60.11	19.25	9.22
highly unsaturated	0.9-1	> 0.5	5.9	2.4	0.1	2.24	1.61	0.12

Table S5: Intensity of exemplary core (C_0) and alkylated (C_1) condensed aromatic compounds identified by APPI FT-ICR MS in sample N07 potentially impacted by gas flaring.

Sum Formula	Intensity [a.u.]		C0 / (C0+C1)	tentative assigned molecule
	C0	C1		
C20H12	8.03E+06	2.03E+06	0.80	Benzofluoranthene, Benzopyrene, Perylene
C22H12	8.31E+06	1.73E+06	0.83	Anthanthrene, Benzo[ghi]perylene
C17H10O	1.45E+07	5.49E+06	0.73	Benzanthrone
C18H10O	2.68E+06	4.65E+06	0.37	Pyreno[1,2-b]furan, Chryseno[4,5-bcd]furan
C19H10O	1.05E+07	6.01E+06	0.64	4H-Cyclopenta(def)chrysen-4-one, Benzo[cd]pyren-5-one

Table S6: Sum parameter from FT-ICR MS measurements of aerosol samples from Bely Island with a sampling duration of one week each.

sum parameter	B01			B02			B03		
	int. weighted average			int. weighted average			int. weighted average		
	APPI	ESI-	ESI+	APPI	ESI-	ESI+	APPI	ESI-	ESI+
number	4586	3553	6987	5231	2817	7361	552	396	754
OSc	-0.61	-0.32	-0.78	-0.75	-0.47	-0.81	-1.20	-0.89	-1.17
DBE	7.09	6.75	6.01	6.87	6.15	6.19	4.74	7.14	6.49
AI	0.20	0.16	0.11	0.20	0.15	0.09	0.18	0.25	0.15
log(C*)	-5.19	-4.99	-5.87	-4.02	-4.01	-6.60	-1.26	-8.61	-6.31
OM/OC	2.90	2.96	3.01	2.83	2.97	3.00	2.82	2.86	2.91
H/C	1.44	1.40	1.58	1.45	1.45	1.59	1.61	1.49	1.64
O/C	0.42	0.54	0.40	0.35	0.49	0.39	0.22	0.32	0.26
N/C	0.08	0.08	0.06	0.07	0.08	0.06	0.13	0.07	0.06
S/C	0.05	0.07	0.05	0.04	0.07	0.04	0.05	0.04	0.04
O/N	6.65	8.39	6.83	6.54	8.06	7.15	3.06	4.28	4.10
O/S	11.43	9.86	3.69	9.13	8.17	4.98	9.14	5.14	4.32
C	21.09	18.62	23.31	22.14	18.52	25.09	21.41	28.87	28.66
H	30.77	26.16	37.20	32.97	27.10	40.30	35.48	46.91	47.16
N	0.76	0.43	0.60	0.43	0.36	0.50	0.16	1.44	0.81
O	7.68	9.31	8.31	6.80	8.35	8.68	3.64	6.12	5.31
S	0.07	0.07	0.03	0.01	0.07	0.02	0.02	0.38	0.18
m/z	420.82	405.79	474.08	414.87	389.38	504.90	354.66	523.02	512.13

Table S7: Summed relative intensity of compound classes in the main wildfire (WF) impacted samples (N01–N05) and ambient aerosol (AA) at Nadym (N09) as well as a wildfire impacted sample on Bely Island (B01).

Ionization	Sample	relative Intensity [%]						
		CH	CHO	CHNO	CHOS	CHNOS	CHN	CHNS
APPI	Nadym-WF	0.4	52.0	45.9	0.0	1.1	0.0	0.0
	Bely-WF	0.2	64.0	34.8	0.0	0.4	0.0	0.0
	Nadym-AA	4.6	80.8	9.5	0.7	4.3	0.0	0.0
ESI-	Nadym-WF	0.0	50.3	36.1	5.4	7.7	0.1	0.1
	Bely-WF	0.0	66.3	26.7	4.7	2.2	0.0	0.1
	Nadym-AA	0.6	46.8	39.2	7.4	4.9	0.5	0.4
ESI+	Nadym-WF	0.0	50.0	46.2	0.7	2.0	1.3	0.8
	Bely-WF	0.0	59.0	39.0	0.5	1.1	0.1	0.1
	Nadym-AA	0.0	58.5	27.1	9.2	3.3	1.1	0.5

Table S8: Ratios of primary and pyrolytic retene in aerosol samples from this study, with comparison to reported ratios from literature.

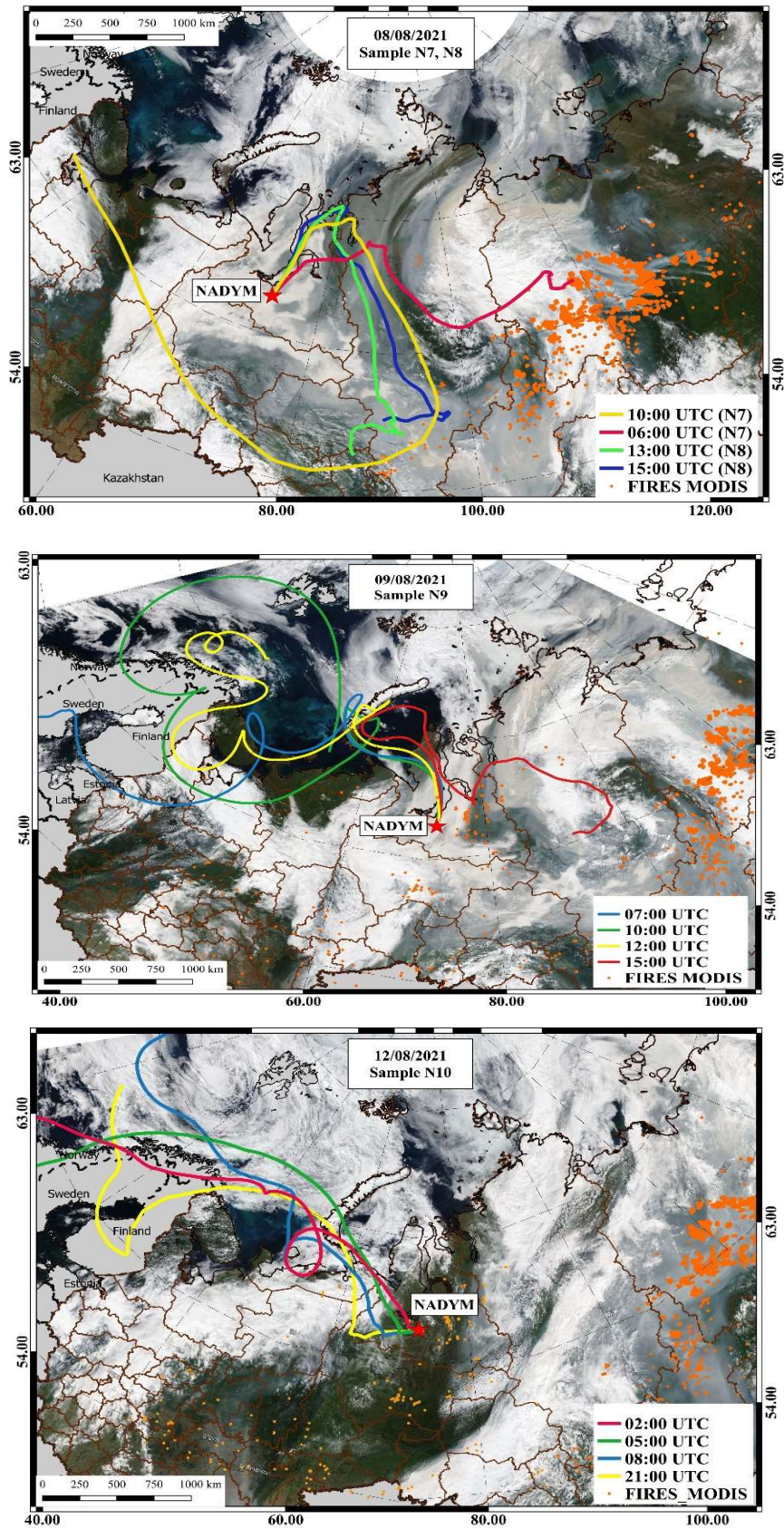| Reference	Sample	RET_{prim}/RET_{pyr}	Comment
this study	N01	0.00	
	N02	0.02	
	N03	0.25	
	N04	0.15	
	N05	0.18	
	N07	0.26	
	N08	0.00	
	N09	0.00	
	N10	0.00	
	B01	0.09	
	B02	0.07	
	B03	n.a.	no RETprim and RETpyr detected
(Czech et al., 2018)	sp1	0.49	
	sp2	0.79	
	sp3	0.80	
	sp*	0.29	slow ignition, intermediate smoldering
(Miersch et al., 2019b)	exp1	0.51	
	exp2	0.71	
	exp3	0.75	
	exp4	0.63	
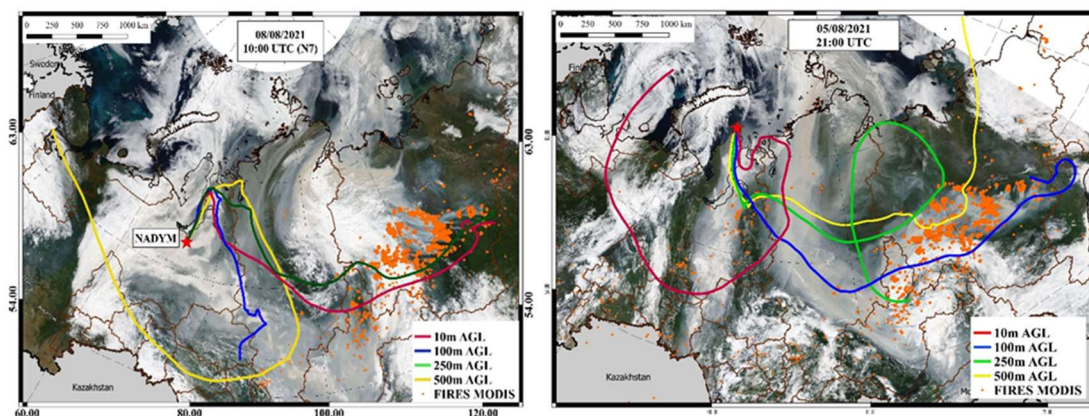
Figure S1: Air mass backward trajectories (10 days back) and satellite image of smoke plume at corresponding times of all samples collected in Nadym (left) and Bely (right). The maps were created using Open Source Geographic Information System QGis (https://qgis.org/en/site) with satellite imagery with TERRA MODIS fire anomaly layer and The MODIS Corrected Reflectance true color imagery as the base layer. (MODIS Science Team, 2017a, 2017b, 2017c, 2017d) Open-source Natural_Earth_quick_start package was used to add a layer of natural and cultural boundaries and polygons from ESRI Shapefile storage. Backward trajectories were calculated using HYSPLIT software (https://www.ready.noaa.gov/HYSPLIT.php) for both Nadym (08/08/2021) and Bely Island (05/08/2021) at the range of altitudes of 10 m, 100 m, 250 m and 500 m. One can see that air mass transportation at any altitude including 10 m took place through the smoke plume covered the large territory of Western Siberia, BWT arrived to the station site from the same direction.

05/08/2021
Sample N1

NADYM

- 10:00 UTC
- 11:00 UTC
- 12:00 UTC
- FIRES MODIS

06/08/2021
Sample N2

NADYM

- 04:00 UTC
- 06:00 UTC
- 08:00 UTC
- FIRES MODIS

07/08/2021
Sample N3, N4, N5

NADYM

- 05:00 UTC
- 07:00 UTC
- 09:00 UTC
- 15:00 UTC
- 17:00 UTC
- FIRES MODIS
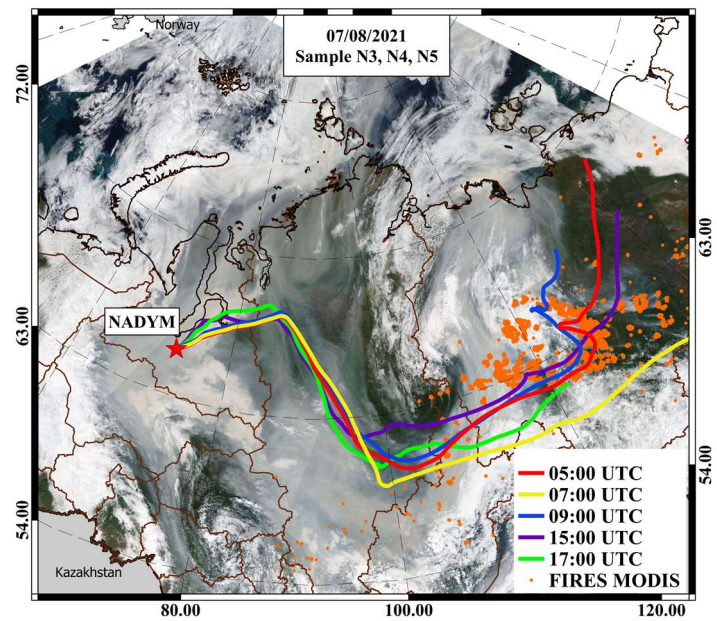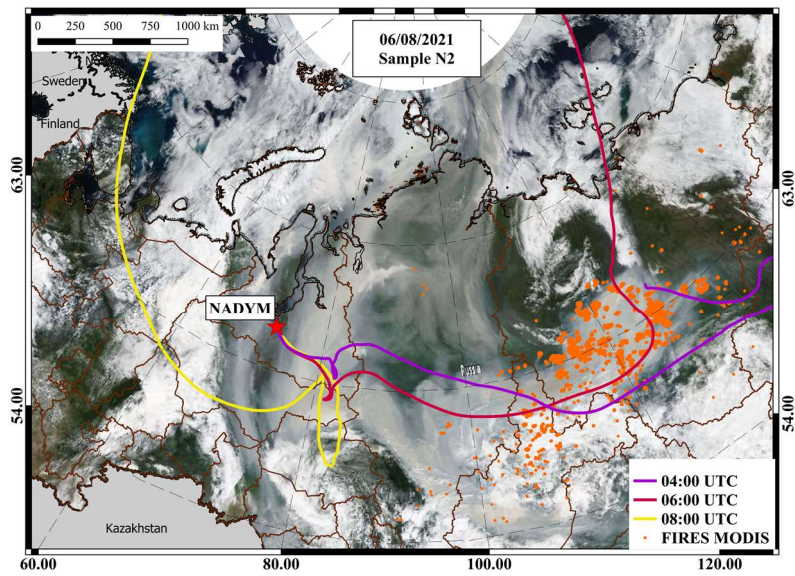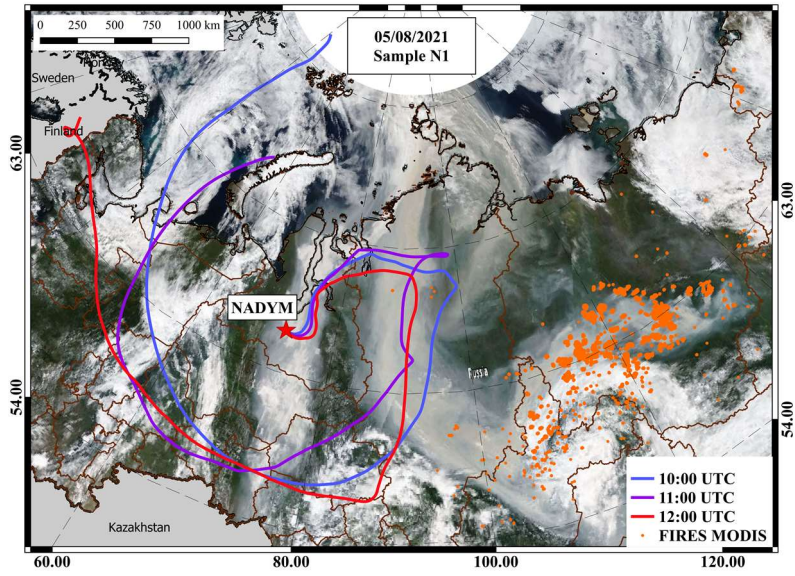
Figure S2 Air mass backward trajectories (10 days back) and satellite image of smoke plume at corresponding times of all samples collected in Nadym. The maps were created using Open Source Geographic Information System QGis (https://qgis.org/en/site) with satellite imagery

with TERRA MODIS fire anomaly layer and The MODIS Corrected Reflectance true color imagery as the base layer. (MODIS Science Team, 2017a, 2017b, 2017c, 2017d) Open-source Natural_Earth_quick_start package was used to add a layer of natural and cultural boundaries and polygons from ESRI Shapefile storage. Backward trajectories were calculated using HYSPLIT software (https://www.ready.noaa.gov/HYSPLIT.php).
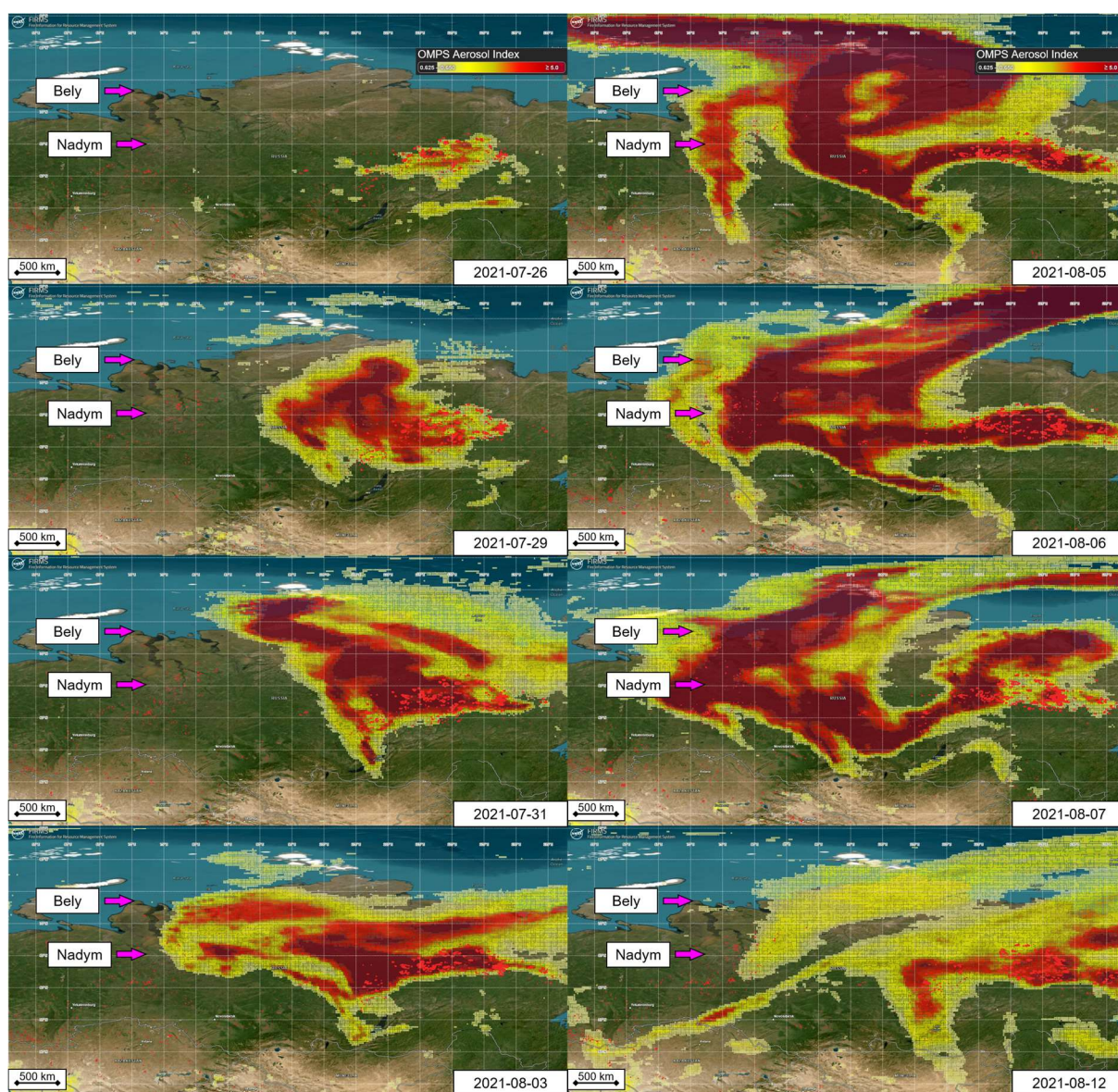
Figure S3 Satellite images of evolving wildfire plume over Siberia with sampling locations indicated by purple arrows. Active fires indicated by red dots, taken from MODIS Terra (Fire and Thermal Anomalies, https://firms.modaps.eosdis.nasa.gov/map). OMPS Aerosol Index (OMPS_NPP_NMMIEAI_L2) displayed by yellow–red colorbar, indicating the presence of ultraviolet-absorbing particles (e.g., a wildfire plume) (Torres, 2019).
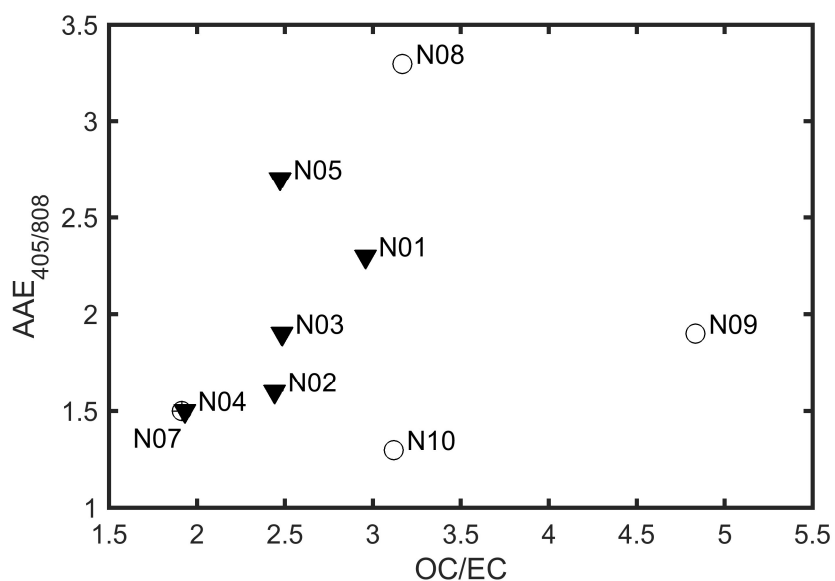
Figure S4: Plot of the organic carbon (OC) to elemental carbon (EC) ratio versus the $AAE_{405/808}$ values determined by the thermal-optical carbon analyzer of filter samples collected in Nadym city with a correlation coefficient of 0.59. Sample assigned to the main plume period are indicated by black triangles (N01–N05), and samples after the main plume period by white circles (N08–N10).
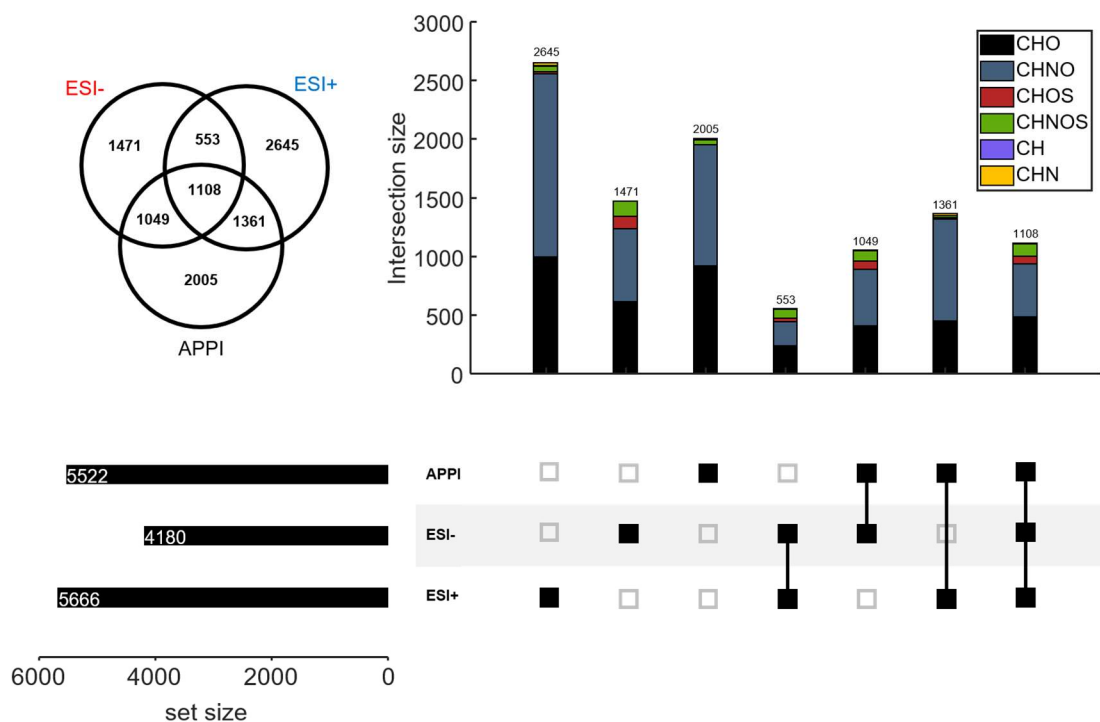
Figure S5: Venn diagram and upset plot of sum formulae identified by the three applied ionization techniques atmospheric pressure photoionization (APPI), negative electrospray ionization (ESI-) and ESI+ in the main wildfire plume impacted samples (N01–N05). Compound class distribution of each Venn-diagram intersection displayed by the setup plot.
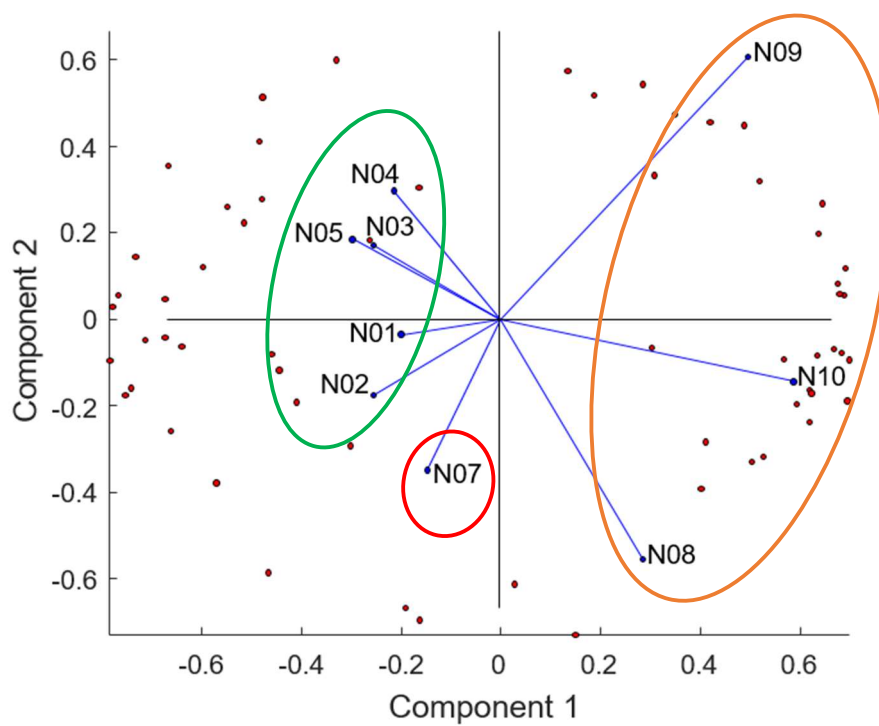
Figure S6: Principal component biplot results of sum parameters (Table S3) from all three FT-ICR MS ionization techniques.
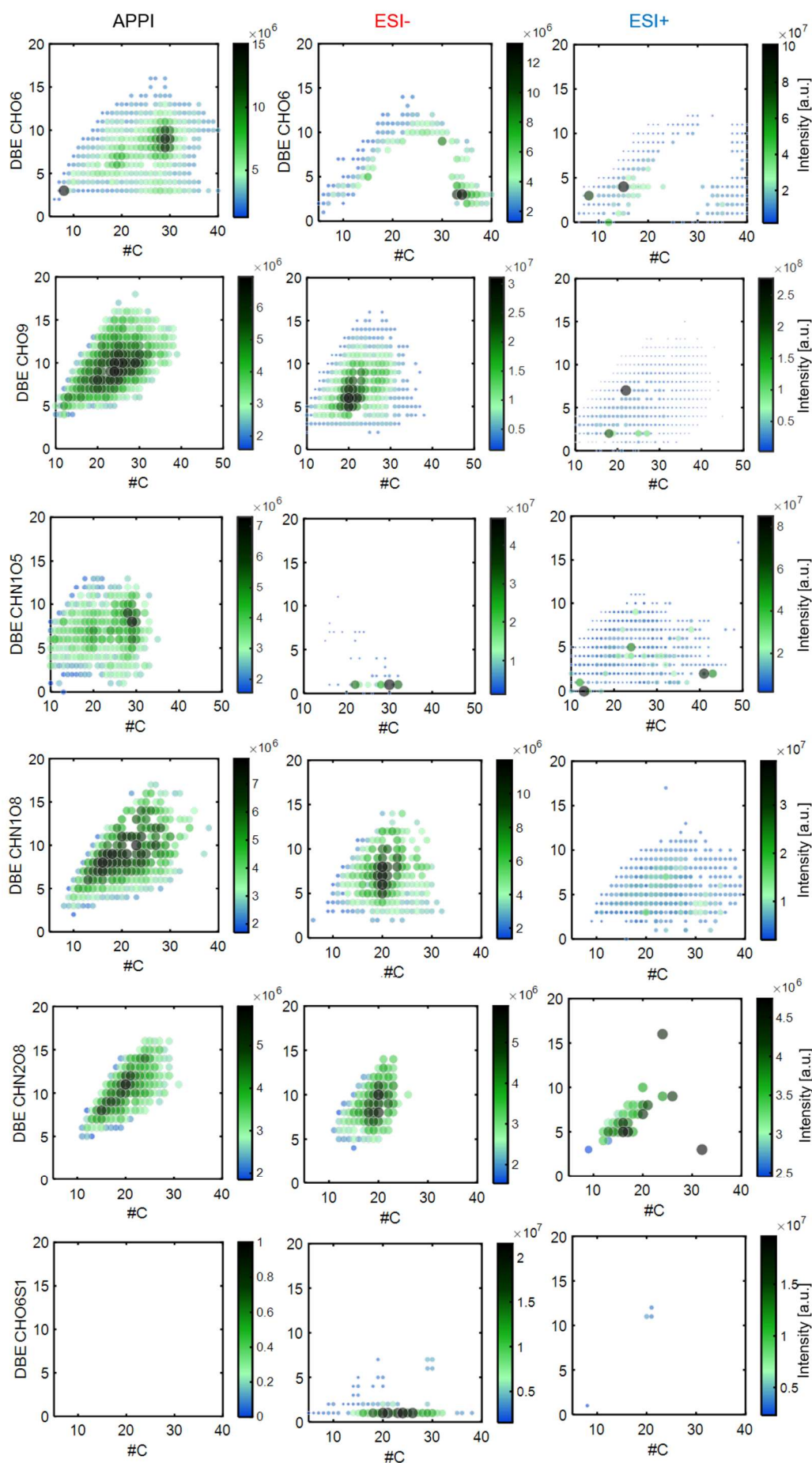
Figure S7: DBE versus carbon number plot for selected compound classes in each applied ionization technique for averaged main wildfire impacted samples (N01–N05). Signal intensity indicated by colour scale and dot size.
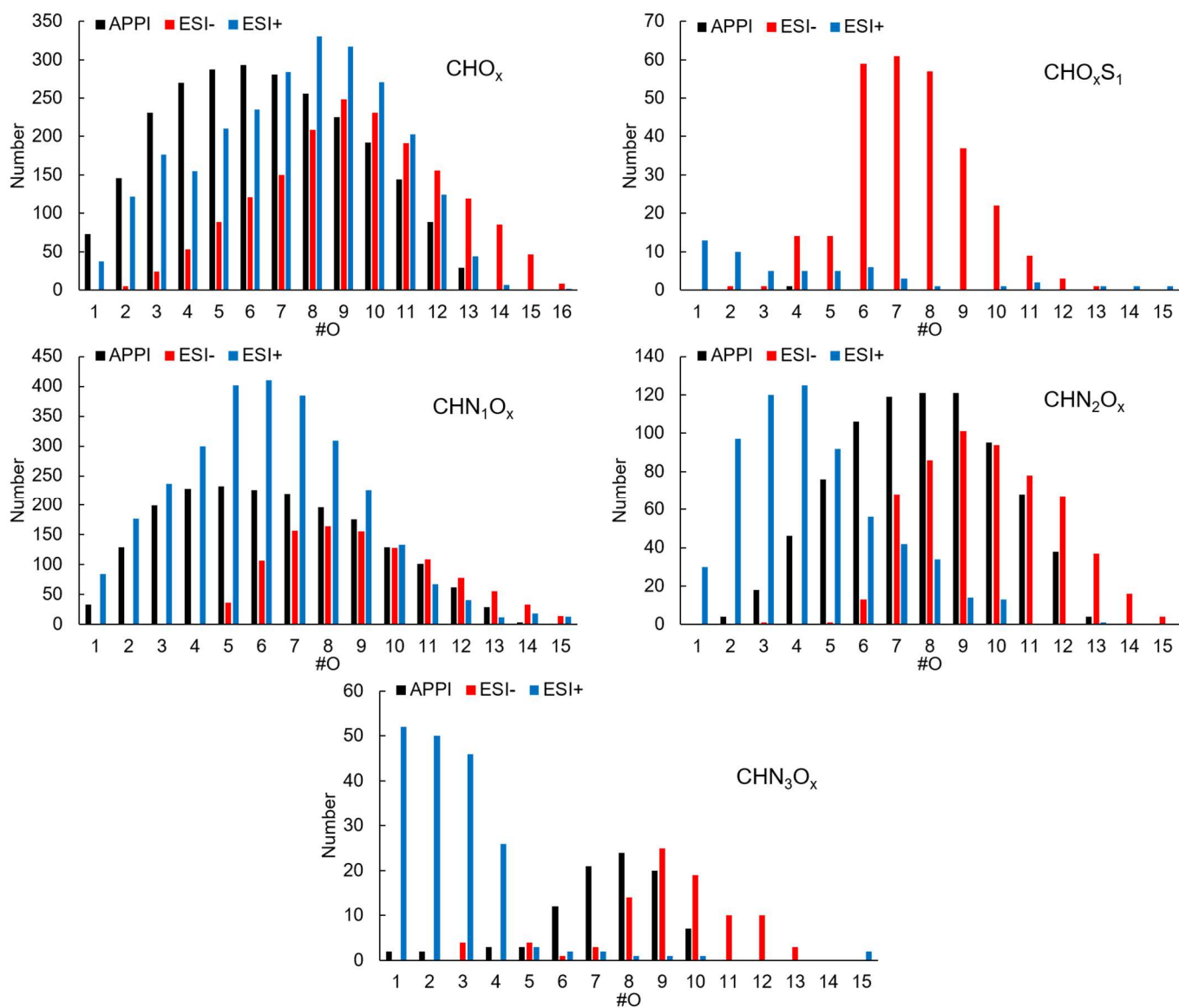
Figure S8: Oxygen number distribution of assigned elemental compositions in APPI (black), ESI- (red) and ESI+ (blue) per compound class for averaged wildfire impacted samples at Nadym (N01-N05).
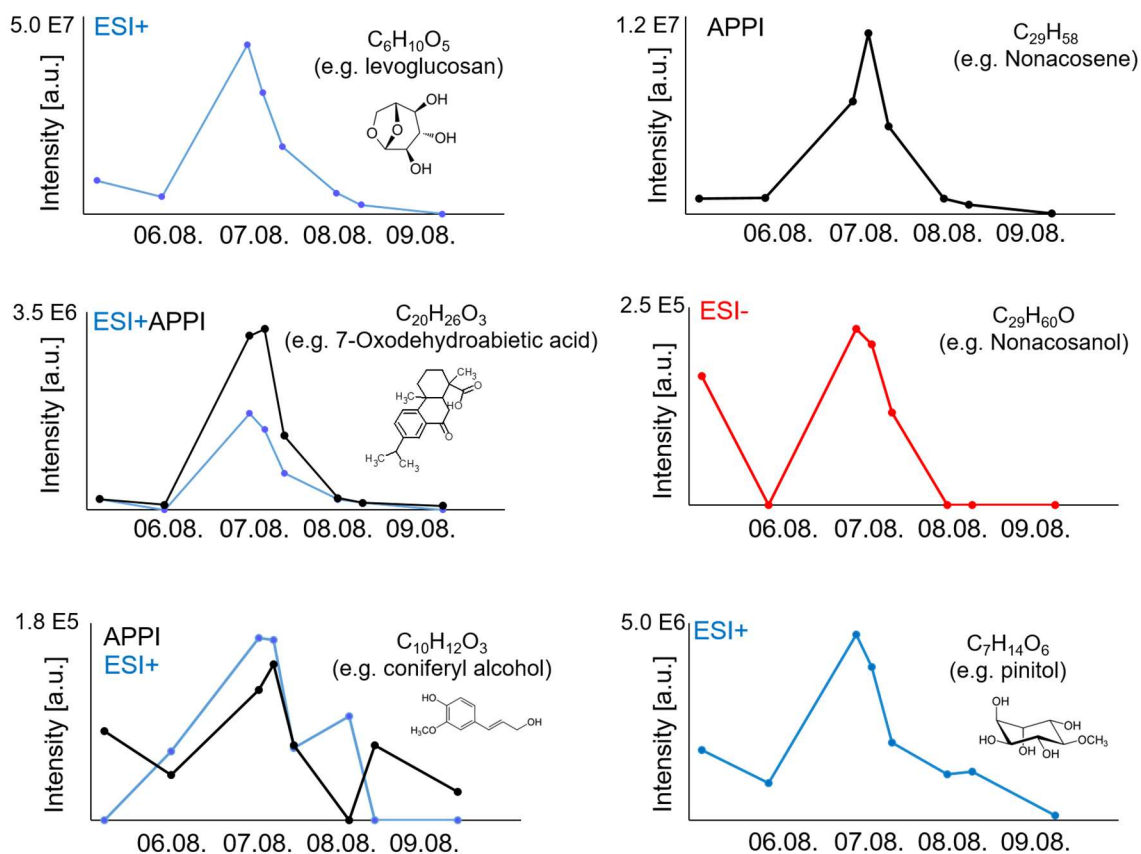
Figure S9: Semi-quantitative time trends of selected biomass burning marker elemental compositions, assigned with possible molecular structures, with intensity normalized to sampling volume.
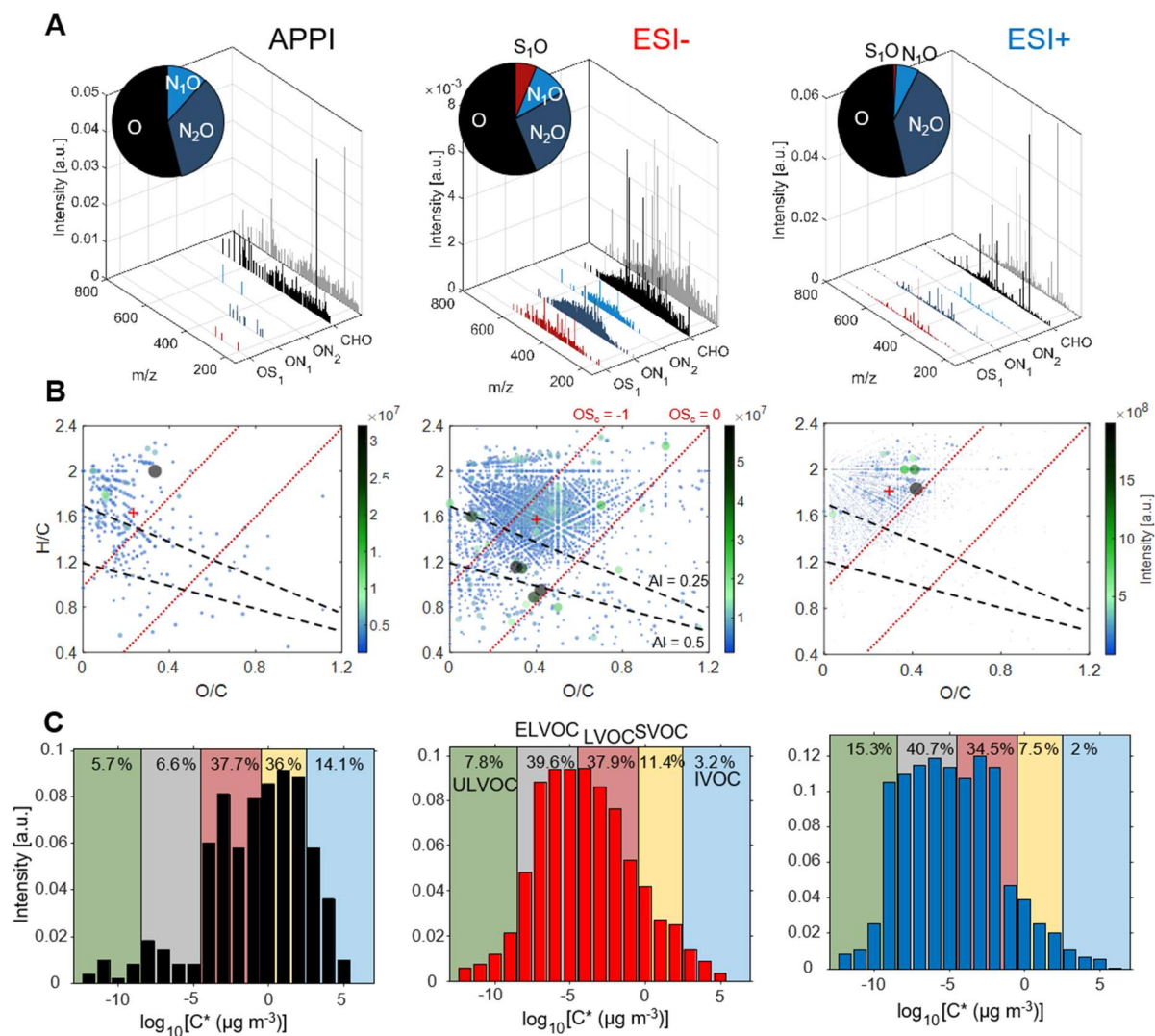
Figure S10: FT-ICR MS data overview. **A**: Normalized mass spectra of sample N09 (ambient aerosol) in three ionization techniques (left to right: APPI, ESI- and ESI+), with insert of relative abundance of the four main compound classes. **B**: Van-Krevelen diagrams with average H/C and O/C ratio marked red. Dotted lines indicate limits of average carbon oxidation state (OS_C, red) and aromaticity index (AI, black) **C**: Saturation vapor pressure distribution with relative intensity of each volatility class given in percent (blue: IVOC, yellow: SVOC, red: LVOC, gray: ELVOC, green: ULVOC).
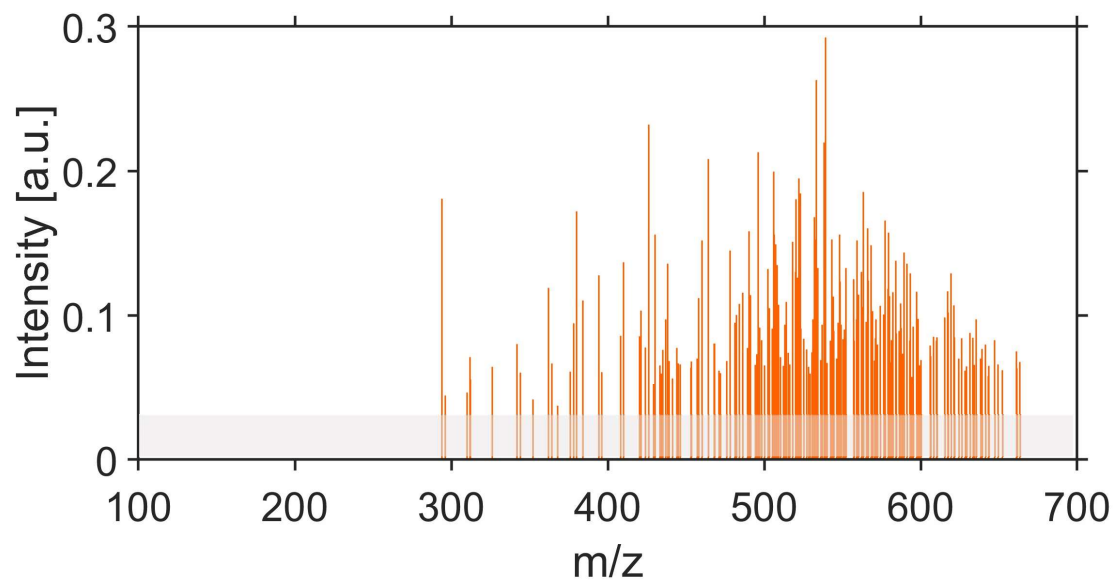
Figure S11: Averaged and normalized assigned elemental composition mass spectra of CHNOS compounds in wildfire plume impacted samples in Nadym (N01–N05) in ESI-. The grey area indicates the intensity threshold for peak picking.
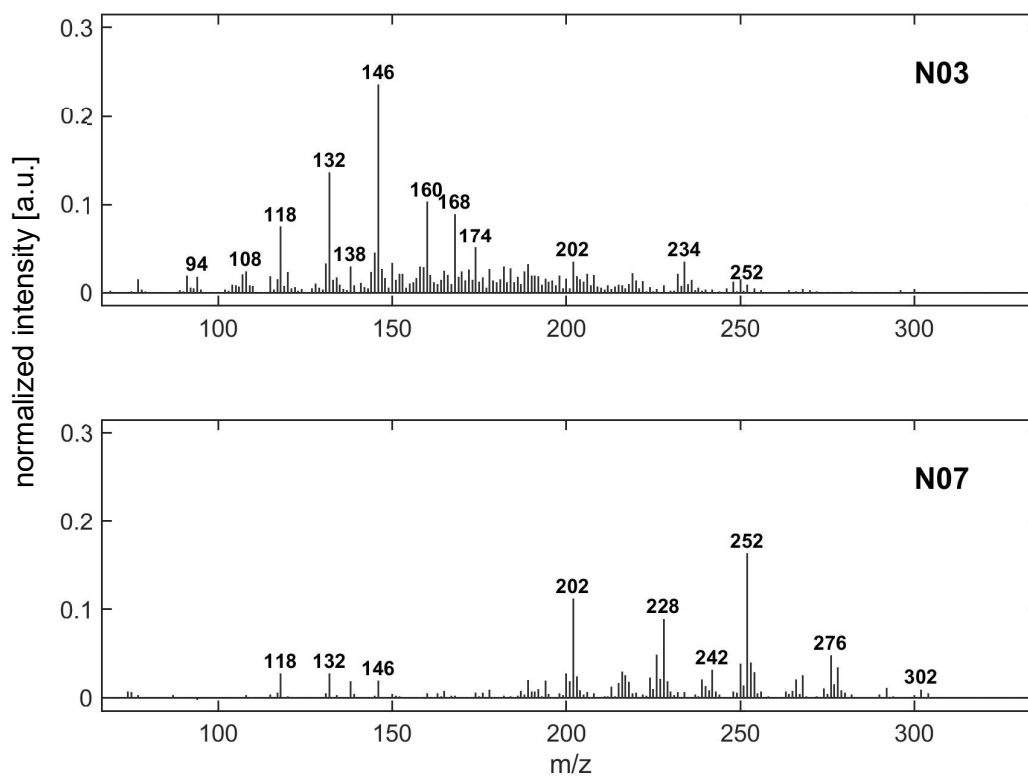
Figure S12: REMPI mass spectra, normalized to sampling volume, of OC12 from Nadym wildfire plume impacted samples N03 (mid of plume period) and N07 (declining plume, also impacted by gas flaring).
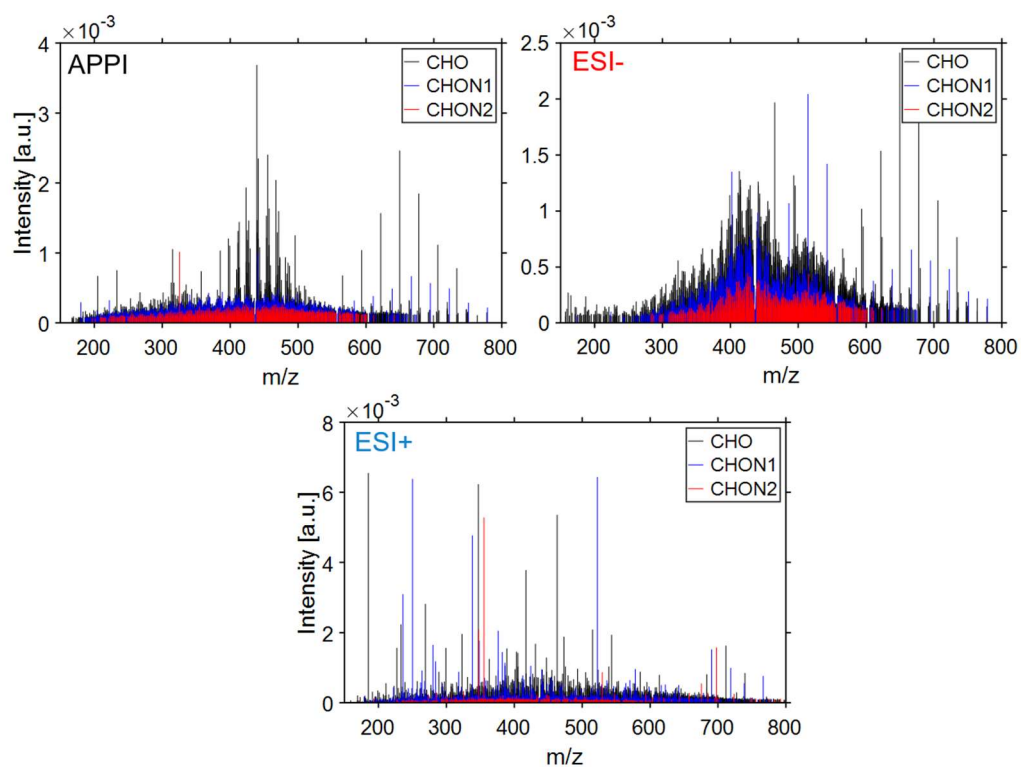
Figure S13: TIC normalized mass spectra of CHO (black), CHN_1O (blue) and CHN_2O (red) compound classes, identified in Nadym wildfire aerosol by APPI (top, left), ESI- (top, right) and ESI+ (bottom).
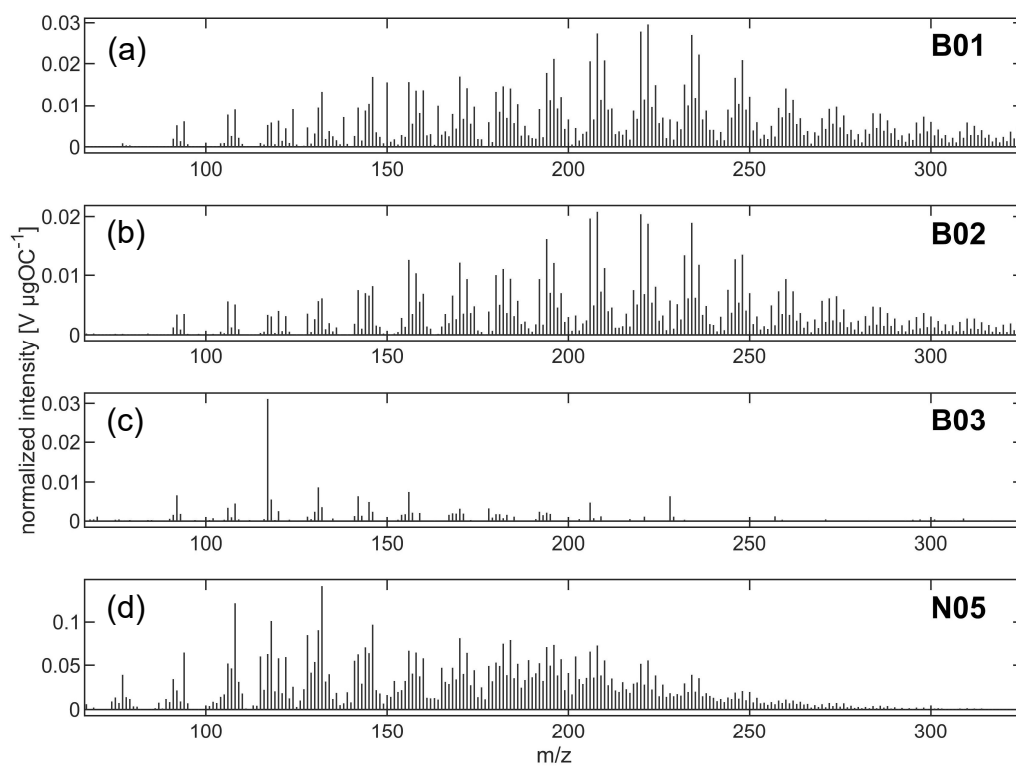
Figure S14: REMPI mass spectra, normalized to sampling volume, of OC12 from Bely wildfire plume impacted samples B01(**a**) and B02 (**b**) as well as B03 (**c**, Bely, ambient aerosol) and N05 (**d**, Nadym plume impacted) for comparison.
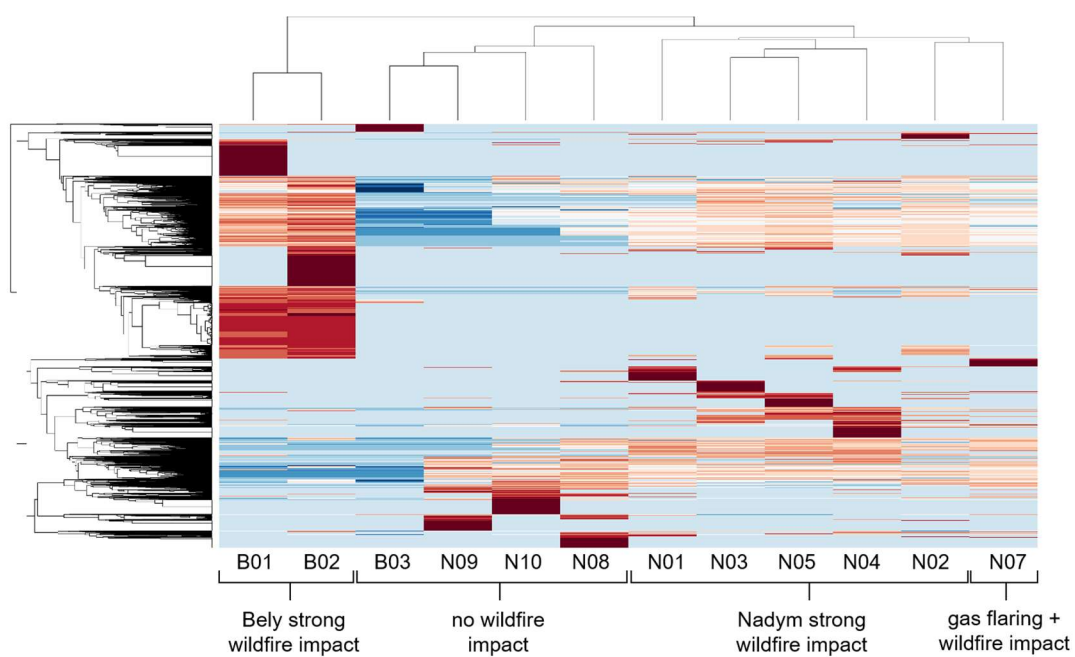
Figure S15: Clustergram of all elemental compositions detected in ESI+ (15,517 compounds) including Nadym and Bely samples (12 samples). Absolute intensity of each elemental compositions normalized by power transformation.
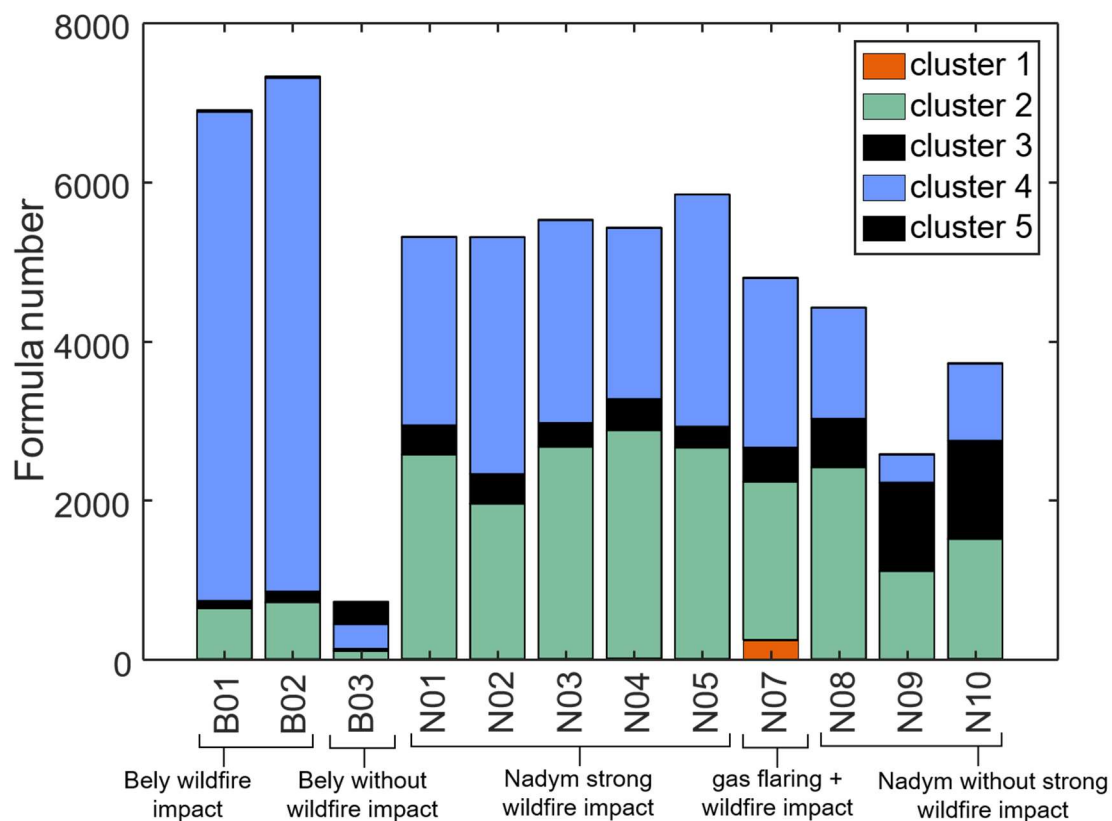
Figure S16: Stacked bar plot of formula number distribution into five clusters by hierarchical cluster analysis of normalized (power transformation) absolute intensities of all elemental compositions identified by ESI+ FT-ICR MS. Cluster 4 (blue) is associated with aged wildfire compounds, cluster 2 (green) is associated with fresh wildfire aerosol, cluster 1 (orange) with gas flaring and cluster 3 and cluster 5 (black) are associated with ambient PM without contribution of wildfires at Bely Island and in Nadym, respectively

References

Cho, M.-H., Park, R. J., Yoon, J., Choi, Y., Jeong, J. I., Labzovskii, L., Fu, J. S., Huang, K., Jeong, S.-J., and Kim, B.-M.: A missing component of Arctic warming: black carbon from gas flaring, Environ. Res. Lett., 14, 94011, https://doi.org/10.1088/1748-9326/ab374d, 2019.

Czech, H., Sippula, O., Kortelainen, M., Tissari, J., Radischat, C., Passig, J., Streibel, T., Jokiniemi, J., and Zimmermann, R.: On-line analysis of organic emissions from residential wood combustion with single-photon ionisation time-of-flight mass spectrometry (SPI-TOFMS), Fuel, 177, 334–342, https://doi.org/10.1016/j.fuel.2016.03.036, 2016.

Czech, H., Miersch, T., Orasche, J., Abbaszade, G., Sippula, O., Tissari, J., Michalke, B., Schnelle-Kreis, J., Streibel, T., Jokiniemi, J., and Zimmermann, R.: Chemical composition and speciation of particulate organic matter from modern residential small-scale wood combustion appliances, The Science of the total environment, 612, 636–648, https://doi.org/10.1016/j.scitotenv.2017.08.263, 2018.

Decker, Z. C. J., Robinson, M. A., Barsanti, K. C., Bourgeois, I., Coggon, M. M., DiGangi, J. P., Diskin, G. S., Flocke, F. M., Franchin, A., Fredrickson, C. D., Gkatzelis, G. I., Hall, S. R., Halliday, H., Holmes, C. D., Huey, L. G., Lee, Y. R., Lindaas, J., Middlebrook, A. M., Montzka, D. D., Moore, R., Neuman, J. A., Nowak, J. B., Palm, B. B., Peischl, J., Piel, F., Rickly, P. S., Rollins, A. W., Ryerson, T. B., Schwantes, R. H., Sekimoto, K., Thornhill, L., Thornton, J. A., Tyndall, G. S., Ullmann, K., van Rooy, P., Veres, P. R., Warneke, C., Washenfelder, R. A., Weinheimer, A. J., Wiggins, E., Winstead, E., Wisthaler, A., Womack, C., and Brown, S. S.: Nighttime and daytime dark oxidation chemistry in wildfire plumes: an observation and model analysis of FIREX-AQ aircraft data, Atmos. Chem. Phys., 21, 16293–16317, https://doi.org/10.5194/acp-21-16293-2021, 2021.

Donahue, N. M., Epstein, S. A., Pandis, S. N., and Robinson, A. L.: A two-dimensional volatility basis set: 1. organic-aerosol mixing thermodynamics, Atmos. Chem. Phys., 11, 3303–3318, https://doi.org/10.5194/acp-11-3303-2011, 2011.

Douben, P. E. T. (Ed.): PAHs: an ecotoxicological perspective, Wiley, Chichester u.a., 2003.

Gehm, C., Streibel, T., Passig, J., and Zimmermann, R.: Determination of Relative Ionization Cross Sections for Resonance Enhanced Multiphoton Ionization of Polycyclic Aromatic Hydrocarbons, Applied Sciences, 8, 1617, https://doi.org/10.3390/app8091617, 2018.

Haefliger, O. P. and Zenobi, R.: Laser mass spectrometric analysis of polycyclic aromatic hydrocarbons with wide wavelength range laser multiphoton ionization spectroscopy, Anal. Chem., 70, 2660–2665, https://doi.org/10.1021/ac971264f, 1998.

Kharuk, V. I., Ponomarev, E. I., Ivanova, G. A., Dvinskaya, M. L., Coogan, S. C. P., and Flannigan, M. D.: Wildfires in the Siberian taiga, Ambio, 50, 1953–1974, https://doi.org/10.1007/s13280-020-01490-x, 2021.

Koch, B. P. and Dittmar, T.: From mass to structure: an aromaticity index for high-resolution mass data of natural organic matter, Rapid Commun. Mass Spectrom., 20, 926–932, https://doi.org/10.1002/rcm.2386, 2006.

Kroll, J. H., Donahue, N. M., Jimenez, J. L., Kessler, S. H., Canagaratna, M. R., Wilson, K. R., Altieri, K. E., Mazzoleni, L. R., Wozniak, A. S., Bluhm, H., Mysak, E. R., Smith, J. D., Kolb, C. E., and Worsnop, D. R.: Carbon oxidation state as a metric for describing the chemistry of atmospheric organic aerosol, Nat. Chem., 3, 133–139, https://doi.org/10.1038/nchem.948, 2011.

Lai, C., Liu, Y., Ma, J., Ma, Q., and He, H.: Laboratory study on OH-initiated degradation kinetics of dehydroabietic acid, Phys. Chem. Chem. Phys., 17, 10953–10962, https://doi.org/10.1039/C5CP00268K, 2015.

Li, Y., Pöschl, U., and Shiraiwa, M.: Molecular corridors and parameterizations of volatility in the chemical evolution of organic aerosols, Atmos. Chem. Phys., 16, 3327–3344, https://doi.org/10.5194/acp-16-3327-2016, 2016a.

Li, Y., Pöschl, U., and Shiraiwa, M.: Molecular corridors and parameterizations of volatility in the chemical evolution of organic aerosols, Atmos. Chem. Phys., 16, 3327–3344, https://doi.org/10.5194/acp-16-3327-2016, 2016b.

Miersch, T., Czech, H., Stengel, B., Abbaszade, G., Orasche, J., Sklorz, M., Streibel, T., and Zimmermann, R.: Composition of carbonaceous fine particulate emissions of a flexible fuel DISI engine under high velocity and municipal conditions, Fuel, 236, 1465–1473, https://doi.org/10.1016/j.fuel.2018.09.136, 2019a.

Miersch, T., Czech, H., Hartikainen, A., Ihalainen, M., Orasche, J., Abbaszade, G., Tissari, J., Streibel, T., Jokiniemi, J., Sippula, O., and Zimmermann, R.: Impact of photochemical ageing on Polycyclic Aromatic Hydrocarbons (PAH) and oxygenated PAH (Oxy-PAH/OH-PAH) in logwood stove emissions, The Science of the total environment, 686, 382–392, https://doi.org/10.1016/j.scitotenv.2019.05.412, 2019b.

MODIS Science Team: MOD021KM MODIS/Terra Calibrated Radiances 5-Min L1B Swath 1km, 2017a.

MODIS Science Team: MOD02HKM MODIS/Terra Calibrated Radiances 5-Min L1B Swath 500m, 2017b.

MODIS Science Team: MOD02QKM MODIS/Terra Calibrated Radiances 5-Min L1B Swath 250m, 2017c.

MODIS Science Team: MYD02QKM MODIS/Aqua Calibrated Radiances 5-Min L1B Swath 250m, 2017d.

Northwest Fire Science Consortium: What are? Types of Fire, https://www.nwfirescience.org/sites/default/files/publications/Types%20of%20Fire.pdf, last access: 7 February 2023.

Popovicheva, O. B., Evangeliou, N., Kobelev, V. O., Chichaeva, M. A., Eleftheriadis, K., Gregorič, A., and Kasimov, N. S.: Siberian Arctic black carbon: gas flaring and wildfire impact, Atmos. Chem. Phys., 22, 5983–6000, https://doi.org/10.5194/acp-22-5983-2022, 2022.

Popovicheva, O. B., Engling, G., Ku, I.-T., Timofeev, M. A., and Shonija, N. K.: Aerosol Emissions from Long-lasting Smoldering of Boreal Peatlands: Chemical Composition, Markers, and Microstructure, Aerosol Air Qual. Res., 19, 484–503, https://doi.org/10.4209/aaqr.2018.08.0302, 2019.

Popovicheva, O. B., Evangeliou, N., Eleftheriadis, K., Kalogridis, A. C., Sitnikov, N., Eckhardt, S., and Stohl, A.: Black Carbon Sources Constrained by Observations in the Russian High Arctic, Environ. Sci. Technol., 51, 3871–3879, https://doi.org/10.1021/acs.est.6b05832, 2017.

Romanov, A. A., Tamarovskaya, A. N., Gusev, B. A., Leonenko, E. V., Vasiliev, A. S., and Krikunov, E. E.: Catastrophic PM2.5 emissions from Siberian forest fires: Impacting factors analysis, Environmental pollution (Barking, Essex 1987), 306, 119324, https://doi.org/10.1016/j.envpol.2022.119324, 2022.

Streibel, T., Hafner, K., Mühlberger, F., Adam, T., and Zimmermann, R.: Resonance-enhanced multiphoton ionization time-of-flight mass spectrometry for detection of nitrogen containing aliphatic and aromatic compounds: resonance-enhanced multiphoton ionization spectroscopic investigation and on-line analytical application, Appl. Spectrosc., 60, 72–79, https://doi.org/10.1366/000370206775382767, 2006.

Tautenhahn, S., Lichstein, J. W., Jung, M., Kattge, J., Bohlman, S. A., Heilmeier, H., Prokushkin, A., Kahl, A., and Wirth, C.: Dispersal limitation drives successional pathways in Central Siberian forests under current and intensified fire regimes, Global Change Biol., 22, 2178–2197, https://doi.org/10.1111/gcb.13181, 2016.

Tomshin, O. A. and Solovyev, V. S.: Detection of burnt areas in Yakutia on long-term NOAA satellites data (1985-2015), 288, https://doi.org/10.1117/12.2504569, available at: https://www.spiedigitallibrary.org/conference-proceedings-of-spie/10833/2504569/Detection-of-burnt-areas-in-Yakutia-on-long-term-NOAA/10.1117/12.2504569.full, 2018.

Torres, O. O.: OMPS-NPP L2 NM Aerosol Index swath orbital, 2019.

Zhang, Y., Wang, K., Tong, H., Huang, R.-J., and Hoffmann, T.: The maximum carbonyl ratio (MCR) as a new index for the structural classification of secondary organic aerosol components, Rapid Commun. Mass Spectrom., 35, e9113, https://doi.org/10.1002/rcm.9113, 2021.

Zhu, C., Kanaya, Y., Takigawa, M., Ikeda, K., Tanimoto, H., Taketani, F., Miyakawa, T., Kobayashi, H., and Pisso, I.: FLEXPART v10.1 simulation of source contributions to Arctic black carbon, Atmos. Chem. Phys., 20, 1641–1656, https://doi.org/10.5194/acp-20-1641-2020, 2020.